



**HAL**  
open science

# Multi-scale modelling of a large scale shell-and-tube latent heat storage system for direct steam generation power plants

Clément Beust, Erwin Franquet, Jean-Pierre Bédécarrats, Pierre Garcia,  
Jérôme Pouvreau, Jean-François Fourmigué

## ► To cite this version:

Clément Beust, Erwin Franquet, Jean-Pierre Bédécarrats, Pierre Garcia, Jérôme Pouvreau, et al.. Multi-scale modelling of a large scale shell-and-tube latent heat storage system for direct steam generation power plants. SOLARPACES 2019: International Conference on Concentrating Solar Power and Chemical Energy Systems, Oct 2019, Daegu, France. pp.190002, 10.1063/5.0028816 . hal-04637528

**HAL Id: hal-04637528**

**<https://univ-pau.hal.science/hal-04637528>**

Submitted on 6 Jul 2024

**HAL** is a multi-disciplinary open access archive for the deposit and dissemination of scientific research documents, whether they are published or not. The documents may come from teaching and research institutions in France or abroad, or from public or private research centers.

L'archive ouverte pluridisciplinaire **HAL**, est destinée au dépôt et à la diffusion de documents scientifiques de niveau recherche, publiés ou non, émanant des établissements d'enseignement et de recherche français ou étrangers, des laboratoires publics ou privés.

RESEARCH ARTICLE | DECEMBER 11 2020

## Multi-scale modelling of a large scale shell-and-tube latent heat storage system for direct steam generation power plants **FREE**

Clément Beust; Erwin Franquet; Jean-Pierre Bédécarrats; Pierre Garcia ✉; Jérôme Pouvreau; Jean-François Fourmigué



*AIP Conf. Proc.* 2303, 190002 (2020)

<https://doi.org/10.1063/5.0028816>



**APL Energy**

**Latest Articles Online!**

**Read Now**



# Multi-Scale Modelling of a Large Scale Shell-and-Tube Latent Heat Storage System for Direct Steam Generation Power Plants

Clément Beust<sup>1,2</sup>, Erwin Franquet<sup>2</sup>, Jean-Pierre Bédécarrats<sup>2</sup>, Pierre Garcia<sup>1,a)</sup>, Jérôme Pouvreau<sup>1</sup>, Jean-François Fourmigué<sup>1</sup>

<sup>1</sup>Univ. Grenoble Alpes, CEA, LITEN, DTBH, Thermal Storage Laboratory, 17 avenue des Martyrs, 38054 GRENOBLE Cedex 9, France

<sup>2</sup>Univ. Pau & Pays Adour / E2S UPPA, Laboratoire de Thermique, Energétique et Procédés – IPRA, EA 1932, Bâtiment d'Alembert, Rue Jules Ferry, BP 7511, 64075 PAU Cedex, France

<sup>a)</sup>Corresponding author: pierre.garcia@cea.fr

**Abstract.** The ability of Phase-Change Materials (PCM) to store steam at a constant or almost constant temperature makes them attractive for the heat storage systems of Direct Steam Generation (DSG) solar plants. The design of a shell-and-tube PCM storage module requires to know the influence on heat transfer of the natural convection movements in the liquid PCM. This work presents a multi-scale modelling approach of a storage module taking into account the effects of these small-scale movements in a module-scale design model. A fine 3D model of the PCM fusion during steam charge is used to establish a local 1D correlation for the heat transferred between the liquid water / steam heat transfer fluid (HTF) inside the tubes, and the PCM outside the tubes. A generic design model is then built using this correlation. The methodology was tested on the case of a prototype scale storage module available at CEA Grenoble. The design model reproduces the heat transfer rate predicted by the CFD model, and measured experimentally during a test charge, while allowing 10 to 90 times shorter computational times than the CFD model.

## INTRODUCTION

Direct Steam Generation (DSG) solar plants are Concentrated Solar Power (CSP) plants which use water as Heat Transfer Fluid (HTF): steam is generated directly in the absorber tubes by evaporating liquid water. This technology allows to overcome the temperature limit, around 400°C, imposed by the thermal oils used as HTF in the classic linear-focus CSP plants. It also eliminates the need for a heat exchanger between the HTF and the steam that is fed to the turbine; this reduces the complexity of the plant and allows to reach a higher overall efficiency<sup>1,2</sup>. The heat storage system for a DSG plant should be adapted to the two-phase nature of the liquid water / steam HTF. Research attention is focused on the development of storage technologies using Phase-Change Materials (PCM), which store the thermal energy of the steam at a constant or almost constant temperature, by undergoing a solid-liquid phase transition. The use of PCM allows to minimize the steam pressure drop between charge and discharge; this would not be possible using a sensible heat storage material.<sup>3</sup> Storage systems based on PCM are called Latent Heat Storage (LHS) systems. The most mature LHS technology to date is the shell-and-tube concept<sup>4,5</sup>, in which the HTF flows in tubes that go through a tank filled with PCM. Several prototype shell-and-tube LHS modules for steam storage have been built and studied by various groups<sup>6-8</sup>.

During the fusion and the solidification of a PCM, the temperature-induced density gradients can generate natural convection movements in the liquid phase. Convective heat transfer cannot be neglected when designing a storage system, as they can be significant for large scale storage modules<sup>3</sup>. Practically, heat transfer correlations are often used to take into account the effects of convection on the PCM side<sup>9,10</sup>. However, the correlation coefficients are usually fitted on experimental data<sup>11</sup>; when designing a storage module with a novel geometry, experimental data are not

always available. Besides, for the design of a LHS module for steam storage, the heat transfer correlation needs to be 1D along the tubes. Indeed, the thermal power of the storage module depends on the length of the liquid water column at the bottom of the tubes, due to the much higher heat transfer coefficient on the HTF side when it is condensing or boiling. Therefore, a design model should be able to predict the pure liquid/steam and two-phase lengths in the tubes.

The present work proposes a method for building a design model of a shell-and-tube LHS module for steam storage. The methodology is based on a multi-scale approach: both a design model with a coarse mesh and a finer 3D Computational Fluid Dynamics (CFD) model are used. A local heat transfer correlation is built from CFD simulations of the coupled phase change process and liquid movements in the PCM. This correlation is used in the design model to take into account the heat transfer enhancement due to natural convection and to the conductive fins surrounding the tubes. A generic design model of a shell-and-tube storage module was developed, with the purpose of being parametrized using data from the fine CFD model. This multi-scale approach was tested on the case of the steam charge of a prototype scale steam storage module, available at CEA Grenoble. The heat transfer rate between the liquid water / steam HTF and the PCM predicted by the system model was compared to CFD and experimental results, in order to assess the proposed modelling methodology.

## MULTI-SCALE MODELLING APPROACH

A shell-and-tube LHS system is composed of a PCM-filled shell together with a bundle of tubes, often with fins or inserts, going through the PCM. The HTF flows inside the tubes and exchanges heat with the PCM through the external surface of the tubes and fins. The role of fins and inserts is to enhance the heat transfer between the HTF and the PCM, compensating the low thermal conductivity of most of the materials used as PCMs. When the LHS system is used for steam storage, the HTF is a two-phase liquid water / steam. During the charge of a module with vertical tubes, saturated or superheated steam is injected at the top of the tubes; it condenses into liquid by releasing heat to the PCM, while the initially solid PCM melts. During discharge, liquid water is injected at the bottom of the tubes; the liquid PCM releases the previously stored heat, which causes the water to boil, and the PCM to solidify. The HTF pressure is lower during discharge: indeed, to enable a heat exchange with the PCM, the saturation temperature is higher than the PCM phase change temperature during charge, and lower in discharge. The almost constant PCM temperature during phase change allows to minimize the HTF pressure drop between charge and discharge<sup>3</sup>. Fig.1 represents the typical geometry of a tube with horizontal circular fins and the PCM surrounding it.

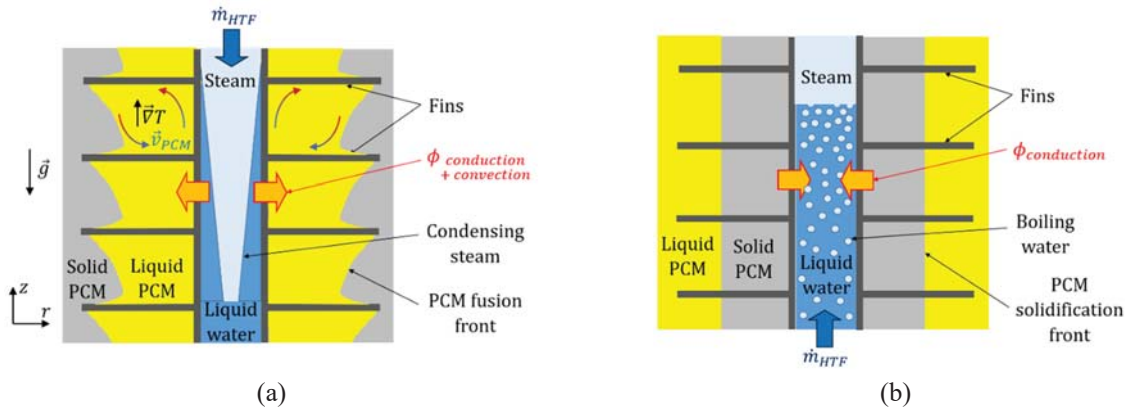


**FIGURE 1.** Schematics of the various physical phenomena occurring in a shell-and-tube latent heat steam storage  
(a) Storage charge – (b) Storage discharge

The physical phenomena that drive the heat transfer between the HTF and the PCM are the convective heat transfer between the HTF and the internal tube wall, the heat conduction in the PCM, the tube wall, the fins and the inserts, the phase change in the HTF and in the PCM, and the natural convection in the liquid PCM. Depending on the geometry of the fins and the inserts, and on the advancement of the PCM fusion or solidification, the amplitude of the natural convection flow can vary: the convection rolls can be confined between adjacent fins or have a larger vertical extension. These aspects impact the contribution of the liquid PCM flow to heat transfer. Heat transfer by natural convection is often represented by a non-dimensional correlation between a Rayleigh (Ra) and a Nusselt number (Nu), in the following form:

$$Nu = C Ra^n \quad (1)$$

The Rayleigh number characterizes the buoyancy forces that drive the natural convection flow in the liquid PCM. The Nusselt number characterizes the convective heat transfer between the inner tube wall and the PCM. The following definitions can be adopted for these two non-dimensional numbers:

$$Ra = \frac{g\beta}{\nu D} (T_w - T_{PCM}) l_c^3 \quad (2)$$

$$Nu = \frac{\phi}{S(T_w - T_{PCM})} \frac{l_c}{\lambda} \quad (3)$$

In these equations,  $\phi$  is the heat flow-rate transferred between the HTF and the PCM (in W) and  $S$  is the associated heat exchange surface (in  $m^2$ ). The temperature difference between the internal tube wall ( $T_w$ ; °C) and the considered fluid ( $T_k$ ) is the driving force of the heat transfer.  $l_c$  is a characteristic length scale of the heat transfer (m).  $g$  is the acceleration of gravity ( $g = 9.81 \text{ m.s}^{-2}$ ). The other terms are physical properties of the fluid:  $\beta$  its thermal expansion coefficient ( $K^{-1}$ ),  $\nu$  its kinematic viscosity ( $m^2.s^{-1}$ ),  $D$  its thermal diffusivity ( $m^2.s^{-1}$ ), and  $\lambda$  its thermal conductivity ( $W.m^{-1}.K^{-1}$ ).

In the literature, correlations of this form are applied to natural convection cases without phase change<sup>12,13</sup>, as well as the flow of the liquid phase of a melting or solidifying PCM<sup>9,11,14</sup>. In the present multi-scale modelling approach, a fine CFD numerical model of the coupled phase change, natural convection flow and heat transfer phenomena on the PCM side is used to predict the heat exchanged between the internal tube wall and the two-phase solid / liquid PCM. Using the results from several carefully chosen CFD computations, a correlation of the form of equation (1) is built for the local heat transfer at a given altitude along the HTF tubes. This correlation is used as an input of a generic system model of a shell-and-tube LHS steam storage system. From the correlation, the system model computes effective conductivity values for the PCM, at each time step and at each point along the tubes. The structure and the features of the multi-scale model are summarized in Fig.2. The CFD and system models are described in detail in the next section.

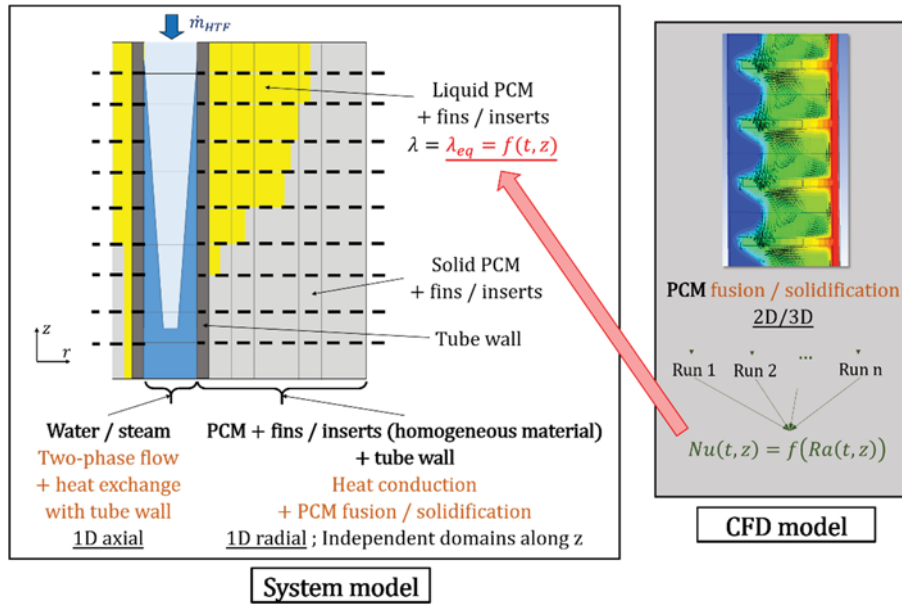


FIGURE 2. Structure and characteristics of the proposed multi-scale model

# SYSTEM AND CFD MODEL DESCRIPTION

## System Model

In the system model, the HTF flow is simulated in 1D in the axial direction. The domain outside the tubes, which contains PCM, fins and inserts, is composed of an array of axisymmetric sub-domains, discretized in 1D in the radial direction. In this domain, the detailed geometry of the fins and inserts is not represented; the PCM, the fins and the inserts are modelled by a unique homogeneous material. The number of sub-domains in the axial direction is equal to the number of HTF mesh cells, each of them being associated to a PCM sub-domain. The axial heat transfer is neglected in the homogeneous material: as depicted by the thick dashed lines on Fig.2, the subdomains are independent of each other. The tube wall is represented by a single column of mesh cells in the axial direction (in dark grey on Fig.2).

The two-phase HTF flow is modelled with a homogeneous approach: the liquid and vapor are assumed to locally share the same temperature and the same velocity. The pressure is assumed not to vary along the tube. In the following equations,  $q_w$  is the heat exchanged with the tube wall,  $\rho_{HTF}$  is the density ( $\text{kg.m}^{-3}$ ; deduced from the HTF pressure and enthalpy),  $t$  is the time (s), and  $\vec{v}$  is the fluid velocity ( $\text{m.s}^{-1}$ ):

$$\frac{\partial \rho_{HTF}}{\partial t} + \vec{\nabla} \cdot (\rho_{HTF} \vec{v}) = 0 \quad (4)$$

$$\frac{\partial (\rho h)_{HTF}}{\partial t} + \vec{\nabla} \cdot (\rho_{HTF} \vec{v} h_{HTF}) - q_w = 0 \quad (5)$$

In a mesh cell denoted with the subscript  $i$ , the heat exchanged  $\varphi_{w,i}$  with the tube wall per surface unit is a function of the difference between the local fluid temperature ( $T_i$ ) and the temperature at the center of the wall ( $T_{w,i}$ ), of the inner and outer radii of the tube (respectively  $R_{in}$  and  $R_e$ ), and of the heat-transfer coefficient  $\alpha_{HTF,i}$  inside the tube:

$$\varphi_{w,i} = \frac{T_{w,i} - T_i}{\frac{R_{in} \cdot \ln\left(\frac{1 + \frac{R_e}{2R_{in}}}{2}\right)}{\lambda_{tube}} + \frac{1}{\alpha_{HTF,i}}} \quad (6)$$

In the tube wall, only the energy balance equation applies. The heat transfer in the axial direction is not neglected. The tube wall temperature appears in the expression of the heat flux between the HTF and the tube wall (equation (6)), and is also used to compute the external tube wall temperature.

Outside the tubes, the solid-liquid transition problem is tackled using the widely-used source-term method<sup>15</sup>, which separates the enthalpy into a sensible and a latent contribution. The energy equation is thus formulated with the sensible enthalpy  $h_{sens}$ , and contains a source term for the heat absorption/release during phase change. The volumic mass change of the PCM when changing phase is not taken into account; the PCM density  $\rho_{PCM}$  is taken constant, equal to its value in the liquid phase. Hereafter,  $Y_l$  is the mass liquid fraction (–),  $L$  is the latent heat of phase change ( $\text{J.kg}^{-1}$ ), and  $x_v$  is the global volume fraction (–) that the PCM occupies in the computational domain. The physical properties and the temperature of the homogeneous material are denoted by the subscript  $h$ , except for the equivalent conductivity  $\lambda_{eq}$ , which involves the natural convection effects and is detailed below.

$$\rho_h \frac{\partial h_{sens}}{\partial t} = \lambda_{eq} \Delta T_h - \rho_{PCM} x_v L \frac{\partial Y_l}{\partial t} \quad (7)$$

The density and heat capacity of the homogeneous material are computed from their values for the pure PCM and metal, assuming that the tube wall and the fins and inserts are made of the same metallic material, and from the volume and mass fractions of the PCM in the computational domain (respectively  $x_v$  and  $x_m$ ):

$$\rho_h = x_v \rho_{PCM} + (1 - x_v) \rho_{metal} \quad (8)$$

$$c_{p,h} = x_m c_{p,PCM} + (1 - x_m) c_{p,metal} \quad (9)$$

The system model follows a finite volume approach, implemented in the Scilab environment. The constitutive equations are discretized using an implicit scheme. At each time step, the problem is first solved on the HTF side with an iterative Newton approach, using the previous tube wall temperature as a boundary condition. Then, the HTF temperature field is used as a boundary condition to solve the problem in the PCM domain and in the tube wall, with the iterative method proposed by Voller et al<sup>15</sup>.

### Method for Calculating an Equivalent PCM Conductivity

The equivalent conductivity  $\lambda_{eq}$  is computed using the  $Nu = f(Ra)$  correlation established using the CFD results, separately for each axial PCM sub-domain (index  $i$ ), and at each time instant. First, it is determined for the layer where the PCM is in liquid phase ( $\lambda_{eq,l,i}$ ), by writing the heat flux  $\Phi_i$  between the external tube wall and the phase change front, using Fourier's law:

$$\phi_i = 2\pi\Delta z\lambda_{eq,l,i} \left( \ln \left( \frac{\sqrt{R_e^2 + (R_{ext}^2 - R_e^2)\bar{Y}_{l,i}}}{R_e} \right) \right)^{-1} (T_{we,i} - T_{pc}) \quad (10)$$

where  $\Delta z$  is the axial space step,  $R_{ext}$  is the outer diameter of the computational domain,  $\bar{Y}_{l,i}$  is the mean mass liquid fraction of the PCM mesh cells in the considered sub-domain,  $T_{we,i}$  is the temperature at the external tube wall in the sub-domain, and  $T_{pc}$  is the phase change temperature. The term  $-R_e + \sqrt{R_e^2 + (R_{ext}^2 - R_e^2)\bar{Y}_{l,i}}$  represents the thickness of the liquid layer in the considered PCM sub-domain. Using equations (3) and (10), the following expression is obtained for  $\lambda_{eq,l,i}$ :

$$\lambda_{eq,l,i} = \lambda_{PCM} \frac{T_{we,i} - T_{PCM,i}}{T_{we,i} - T_{pc}} \frac{R_e}{l_{c,i}} \ln \left( 1 + \frac{-R_e + \sqrt{R_e^2 + (R_{ext}^2 - R_e^2)\bar{Y}_{l,i}}}{R_e} \right) f(Ra_i) \quad (11)$$

where  $Ra_i$  is computed using equation (2), and the function  $f(Ra)$  refers to the correlation between the Nusselt and Rayleigh numbers established with the CFD results

Secondly, an equivalent conductivity is estimated for each mesh cell where the PCM is in solid phase ( $\lambda_{eq,s,i,j}$ ), using the local PCM volume fraction  $x_{v,j}$  as a function of the radius (the index  $j$  refers to the radial position):

$$\lambda_{eq,s,i,j} = x_{v,i,j}\lambda_{PCM} + (1 - x_{v,i,j})\lambda_{metal} \quad (12)$$

where  $\lambda_{PCM}$  and  $\lambda_{metal}$  are the conductivities of pure solid PCM and pure metal (fin and insert material).

Finally, the equivalent conductivity of equation (7) is determined in each mesh cell:

$$\lambda_{eq,i,j} = Y_{l,i,j}\lambda_{eq,l,i} + (1 - Y_{l,i,j})\lambda_{eq,s,i,j} \quad (13)$$

where  $Y_{l,i,j}$  is the local mass liquid fraction in the considered mesh cell. This final expression of the conductivity ensures a smooth transition between the solid and liquid equivalent conductivities, for the mesh cells where  $0 < Y_{l,i,j} < 1$ .

### CFD Model

In contrast to the system model, the CFD model represents the geometry of the fins and the inserts, in order to simulate their impact on the liquid PCM flow. The PCM is modelled using the enthalpy-porosity approach described by Voller and Prakash<sup>16</sup>. The Boussinesq approximation is used to take into account the buoyancy forces driving the natural convection flow. Like in the system model, the volume change at phase change is not represented, and the density  $\rho$  is taken constant. The three conservation equations are given below. In these equations,  $P$  is the pressure (Pa) and  $\mu$  is the dynamic viscosity of the liquid PCM ( $\text{kg}\cdot\text{m}^{-1}\cdot\text{s}^{-1}$ ); the other notations are defined above.

$$\vec{\nabla} \cdot \vec{v} = 0 \quad (14)$$

$$\rho \left( \frac{d\vec{v}}{dt} + \vec{v} \cdot \vec{\nabla} \vec{v} \right) = -\vec{\nabla} P + \vec{\nabla} (\mu \vec{\nabla} \vec{v}) - \rho\beta(T - T_{ref})\vec{g} + A\vec{v} \quad (15)$$

$$\rho c_p \left( \frac{dT}{dt} + \vec{v} \cdot \vec{\nabla} T \right) = \vec{\nabla} (\lambda \vec{\nabla} T) - \rho L \left( \frac{dY_l}{dt} + \vec{v} \cdot \vec{\nabla} Y_l \right) \quad (16)$$

In the momentum equation (15), the damping term  $A\vec{v}$  is equal to  $\vec{0}$  in the liquid phase ( $Y_l=1$ ), and takes large enough values in the solid phase to dominate the other terms, thus canceling the velocity in the solid:

$$A = -A_{mush} \frac{(1-Y_l)^2}{Y_l^3 + B} \quad (17)$$

with  $B = 10^{-3}$ . The factor  $A_{mush}$ , called the mushy zone constant, controls the amplitude of the velocity damping in the mushy zone, where solid and liquid PCM both exist ( $0 < Y_l < 1$ ). In the present work, the value of  $A_{mush}$  has been set previously by confronting the results of CFD calculations to experimental results.

In the tube wall and the fins, only the energy balance applies:

$$\rho c_p \frac{\partial T}{\partial t} = \lambda \Delta T \quad (18)$$

The CFD simulations are made with the ANSYS Fluent® v. 17.2 software.

## RESULTS AND DISCUSSION

### Storage Module Studied

The modelling methodology was tested on a steam charge for a prototype module available at CEA Grenoble. This module is made of a cylindrical shell, filled with approximately 1700 kg of sodium nitrate ( $\text{NaNO}_3$ ) as PCM, and containing a bundle of 19 finned tubes. Sodium nitrate is an inorganic salt whose solid-liquid phase transition takes place on a temperature range of about 3–4°C around 305°C<sup>17</sup>. The rectangular fins are welded to the tubes following a helical pattern (see Fig.3-(a)). The tube length that is immersed in the PCM is 4.08 m when the salt is fully liquid.

The CFD model is 3D and represents an angular sector of 22.5°, corresponding to a single fin (see Fig.3-(b)). Only a tube length of 0.54 m is represented (27 fins), for the sake of limiting the computational time.

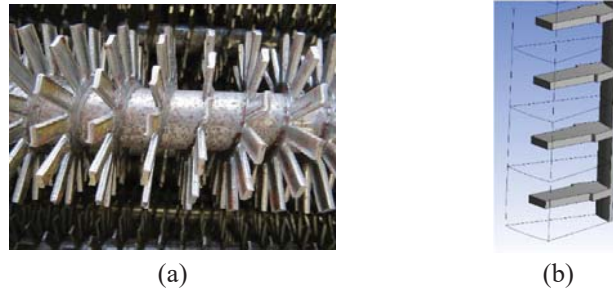


**FIGURE 3.** (a): The finned tubes of the prototype storage module  
(b): Fraction of the computational domain used for the CFD simulation

### CFD Model and Heat Transfer Correlation

The first step of the modelling approach is to identify a correlation of the form of equation (1) for the heat transfer between HTF and PCM, using CFD results. A storage module can be operated so that steam condensation occurs on the whole tube length during the whole charge duration<sup>18</sup>, as this situation minimizes the thermal resistance on the HTF side; the adopted boundary condition reflects such an operating strategy. In the CFD model, a fixed temperature boundary condition is set at the internal tube wall, to represent a situation where the HTF would be two-phase (condensation) on the whole tube length: the HTF temperature is uniform, and the two-phase heat transfer coefficient inside the tube is assumed to be infinite. All the other boundaries of the model are adiabatic (no normal heat flux). The velocity is set to zero at the upper and lower boundaries (no-slip wall condition), and the normal velocity is set to zero at the side and external boundaries (symmetry condition). The material properties adopted in the model are gathered in Table 2 and Table 3, and the other model parameters are gathered in Table 1. The value of  $A_{\text{mush}}$  was set after preliminary calculations when confronting with experimental results from the prototype module. For the PCM mesh cells which contain both solid and liquid ( $0 < Y_l < 1$ ), the sensible thermal capacity  $c_p$  and the conductivity  $\lambda$  are linearly interpolated between the solid and liquid values of Table 2.

**TABLE 1.** Parameters of the CFD model

$A_{\text{mush}}$ ( $\text{kg}\cdot\text{m}^{-3}\cdot\text{s}^{-1}$ )	$T_{\text{ref}}$ ( $^{\circ}\text{C}$ )	Number of mesh cells	Mean space step (mm)	Time step (s)
$10^8$	309	539 046	0.83	0.025 ( $T_w = 328^{\circ}\text{C}$ ) 0.05 ( $T_w = 318^{\circ}\text{C}$ and $310^{\circ}\text{C}$ )

**TABLE 2.** Material properties adopted in the CFD model

Material	$\rho$ ( $\text{kg}\cdot\text{m}^{-3}$ )	$\beta$ ( $\text{K}^{-1}$ )	$c_p$ ( $\text{J}\cdot\text{kg}^{-1}\cdot\text{K}^{-1}$ )	$\lambda$ ( $\text{W}\cdot\text{m}^{-1}\cdot\text{K}^{-1}$ )	$\mu$ ( $\text{kg}\cdot\text{m}^{-1}\cdot\text{s}^{-1}$ )
$\text{NaNO}_3$	1927	$3.8 \times 10^{-4}$	1813 (solid)	0.72 (solid)	0.0028 (liquid)
	(Boussinesq)		1704 (liquid)	0.52 (liquid)	
Steel (tube and fins)	7764	--	542.8	50.33	--

**TABLE 3.** Thermal properties related to the solid-liquid phase transition of NaNO<sub>3</sub> adopted in the CFD model <sup>17</sup>

L (J.kg <sup>-1</sup> )	Phase change temperature interval (°C)
173 300	303.3 - 306.6

For steam charging (PCM fusion), two parameters are expected to influence the heat transferred from the HTF. First, the temperature difference between the external tube wall and the PCM drives the heat transfer, and should also influence the amplitude of the natural convection flow, as it determines the temperature gradient in the liquid PCM. Second, the thickness of the PCM layer influences the room left for the natural convection flow to develop. As this thickness increases during the heat charge when the melting progresses, the CFD computations to run, for establishing the correlation, should be chosen to explore a range of values for the driving temperature difference. Therefore, three CFD computations are led with different tube temperatures:  $T_W = 328^\circ\text{C}$ ,  $318^\circ\text{C}$  and  $310^\circ\text{C}$ . For these computations, the initial temperature is uniform and equal to  $290^\circ\text{C}$ . The independence to the mesh and time step was checked by comparing the results to those obtained with a denser mesh (774098 cells), and those obtained with a smaller time step (0.0125s for  $T_W = 328^\circ\text{C}$ , 0.025s for the two other  $T_W$  values). The time steps were considered converged when the residual values for the five constitutive equations (mass; x,y and z momentum; energy) had dropped by a ratio of  $10^{-3}$  (relative convergence criterion).

The computational domain was divided into 27 sub-domains, each one being centered on an individual fin; the limits of the sub-domains are visible on Fig.3-(b). The heat flux, the molten fraction and the mean liquid PCM temperature were computed at each time step on each sub-domain; these quantities were used to compute Nusselt and Rayleigh numbers according to (2-3), with different definitions for  $l_c$  and  $T_{PCM}$ . Four different definitions for  $l_c$  and three different ones for  $T_{PCM}$  were tried; attempts were made to correlate the Nusselt and Rayleigh numbers for all of the 12 combinations between these parameters. The best correlation was found with  $l_c$  and  $T_{PCM}$  being respectively equal to the length and the mean temperature of the liquid PCM layer, estimated the following way:

$$l_c = -R_e + \sqrt{R_e^2 + (R_{ext}^2 - R_e^2) * \frac{\sum_{i=1}^{nbcells,sub-domains} Y_{l,i} V_i}{\sum_{i=1}^{nbcells,sub-domains} V_i}} \quad (19)$$

$$T_{PCM} = \frac{\sum_{i=1}^{nbcells,sub-domains} \rho c_{p,l} T_i Y_{l,i} V_i}{\sum_{i=1}^{nbcells,sub-domains} \rho c_{p,l} Y_{l,i} V_i} \quad (20)$$

The complete data set of Nusselt and Rayleigh numbers, for the three  $T_W$  values, the 27 fins, and several time instants, is represented on Fig.4. The data points gather around two distinct curves. It was found that the points gather around the lowest curve when the fusion is ongoing ( $l_c < R_{ext} - R_e$  in the considered sub-domain), and around the second curve after the end of the fusion ( $l_c = R_{ext} - R_e$ ). The transition between the two curves happens when the solid PCM layer at the external boundary of the computational domain is replaced by liquid PCM; for the points that lie between the curves on Fig.4, both solid and liquid lie at the external boundary. For these points, as the PCM is locally almost completely melted,  $l_c$  is still strictly inferior but close to  $R_{ext} - R_e$ .

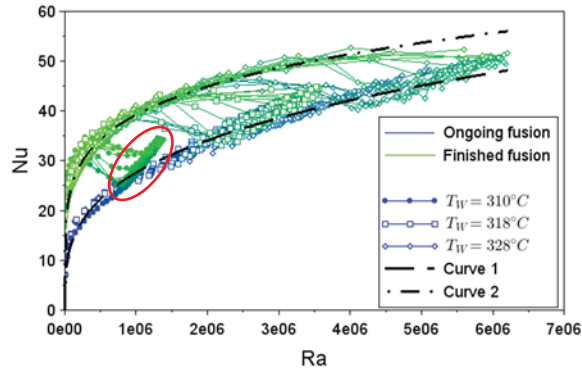


**FIGURE 4.** Scatter plot of the Rayleigh and Nusselt numbers data set, for the chosen definitions of  $l_c$  and  $T_{PCM}$

## Test of the Heat Transfer Correlation in the System Model

The relations found between the Rayleigh and Nusselt numbers were implemented in the system model. At each time step and for each PCM sub-domain in the system model, a characteristic length  $l_{c,i}$  and a liquid temperature  $T_{PCM,i}$  were computed, applying (19-20) to the mesh cells of the system model. This allows to compute a Rayleigh number, and then an equivalent conductivity using (11). For the Nusselt correlation, the transition between the two curves of Fig.4 was arbitrarily set when the mean liquid fraction  $\overline{Y}_{l,i}$  in the considered sub-domain is between 0.98 and 1. The correlation is the following:

$$\begin{cases} Nu_i = 0.402 Ra_i^{0.306}, & 0 < \overline{Y}_{l,i} < 0.98 \\ Nu_i = \frac{\overline{Y}_{l,i} - 0.98}{0.02} (2.614 Ra_i^{0.196}) + \frac{1 - \overline{Y}_{l,i}}{0.02} (0.402 Ra_i^{0.306}), & 0.98 < \overline{Y}_{l,i} < 1 \\ Nu_i = 2.614 Ra_i^{0.196}, & \overline{Y}_{l,i} = 1 \end{cases} \quad (21)$$

Equation (21) constitutes the relation  $Nu = f(Ra)$  that appears in equation (11). In order to assess whether the system model can reproduce the CFD results with this correlation, the three cases with uniform wall temperatures that were simulated with the CFD model were also simulated with the system model. To enforce the desired temperature at the tube wall, the HTF pressure is chosen so that the saturation temperature is equal to the desired wall temperature, and the heat transfer coefficient at the internal tube wall is set to a large value ( $\alpha_{int} = 10^6 \text{ W.m}^{-2}.\text{K}^{-1}$ ). A vapor with a slight superheating of  $0.1^\circ\text{C}$  and an arbitrary mass flow of  $0.05 \text{ kg.s}^{-1}$  is injected at the top of the tube. The other main parameters of the system model are gathered in Table 4.

**TABLE 4.** Parameters adopted for the system model for testing the heat transfer correlation

Tube length (m)	PCM fraction	Mesh subdivisions	Time step (s)	Saturation pressure (bar)
0.54	Mass : $x_m = 0.785$	Axial : 10 ( $\Delta z = 54.0 \text{ mm}$ )	0.025	$T_W = 328^\circ\text{C} : 125.3$
	Volume : $x_v = 0.936$	Radial : 9 ( $\Delta r = 1.85 \text{ mm}$ )		$T_W = 318^\circ\text{C} : 109.9$
				$T_W = 310^\circ\text{C} : 98.65$

The heat stored as a function of time for both models is represented on Fig.5. The two models appear to be in good agreement: the system model correctly reproduces the heat accumulation rate from the CFD, while needing 10 to 40 times shorter computational times than the CFD model to simulate the full PCM melting. The heat charge is predicted to be slightly lower by the system model: the mean discrepancy between the two models during the charge is of 4.8% for  $T_W = 328^\circ\text{C}$ , 6.8% for  $T_W = 318^\circ\text{C}$ , and 14% for  $T_W = 310^\circ\text{C}$ . This effect could be due to the fact that the mushy zone becomes thicker when  $T_W$  decreases. As the liquid flow is damped in the mushy zone, it is likely that when this zone is too thick, the natural convection flow cannot be simply represented by a single layer of pure liquid whose thickness would be defined by equation (19). It can be seen on Fig.4 that for  $T_W = 310^\circ\text{C}$ , there is an important group of points with  $10^6 < Ra < 1.5 \cdot 10^6$  with a higher Nusselt number than predicted by the first correlation curve (circled in red on Fig.4). This shows that the correlation is not fully able to represent natural convection for this case.

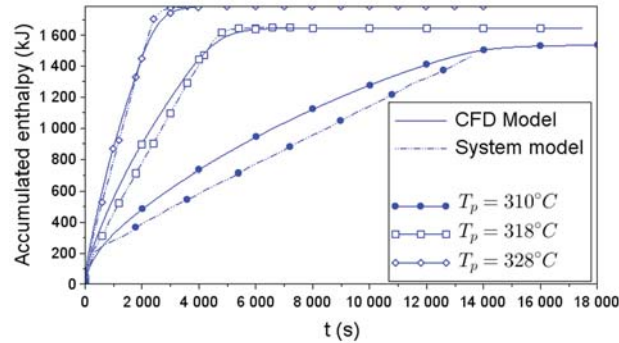


**FIGURE 5.** Enthalpy accumulated in the PCM, the tube and the fins during the heat charge at constant temperature wall

## Validation on Experimental Results

The results of the system model were compared to those obtained experimentally in a test of steam charge that was led on the prototype module. During this test, the HTF pressure was increased continuously from 60.8 bar to 112 bar in 3.5h: the progressive increase of the thermal resistance on the PCM side is compensated by an increase of the saturation temperature of the liquid water / steam, allowing the steam condensation to occur on the whole tube length during the whole charge (sliding pressure operation). Steam is injected with a 1°C superheating and a mass flow-rate of 0.020 kg.s<sup>-1</sup>. The PCM is initially at a uniform temperature of 265°C. For the simulation of this test, the whole tube length (4.08m) was represented in the system model; the PCM mass and volume fractions and the number of mesh subdivisions presented in Table 4 are unchanged ( $\Delta z = 408$  mm here). The adopted time step is 0.25s. The heat transfer coefficient at the internal tube wall was estimated using adapted correlations for single-phase flow<sup>19,20</sup> and two-phase flow<sup>21-23</sup> in a duct.

In the test section, pressure and temperature measurements allow to determine the HTF enthalpy at the inlet and outlet of the prototype module. If the HTF is two-phase at the outlet (steam not fully condensed), the steam mass fraction is determined by condensing the remaining steam in a dedicated condensing device; an enthalpy balance at the condenser allows to estimate an outlet enthalpy. The thermal power that is lost by the HTF when going through the module is deduced from the enthalpy balance between inlet and outlet. Most of this energy is stored in the PCM, the tube and the fins; another part is stored in the other metallic parts that are not represented in the system model, and a last part is lost to the ambient air, at the external walls of the module (heat losses). The energy accumulated in the external wall and in the collectors at the top and the bottom can be estimated, thanks to temperature measurements made in these metallic parts during the test. The thermal losses are estimated thanks to dedicated experimental tests led separately, with a steady case, which allowed to determine a heat loss coefficient. By deducing the contribution of these two effects to the thermal power lost by the HTF, the energy that is stored by the PCM, the tube and the fins only can be estimated. This allows to compare the transient profile of the accumulated energy between the experiment and the model, similarly to what is made on Fig.5 between the CFD and system models.

The evolution of the accumulated energy is plotted on Fig.6, for the experiment (with the two aforementioned effects deduced) and for the CFD and system models. This comparison requires to consider the same mass of PCM and fins. Therefore, for the two models, the accumulated enthalpy is multiplied by the ratio of the total volume of PCM and fins associated to the 19 tubes, to the volume represented in each model. NaNO<sub>3</sub> knows a solid-solid phase transition around 270°C, which is considered in the CFD model (through the dependence of the solid PCM thermal capacity to temperature) but not in the system model. The latent heat value associated to this transition was computed for the PCM mass considered in the system model, and was added to the accumulated energy; for this reason, the curve for the system model on Fig.6 does not start at 0 kJ at t = 0.

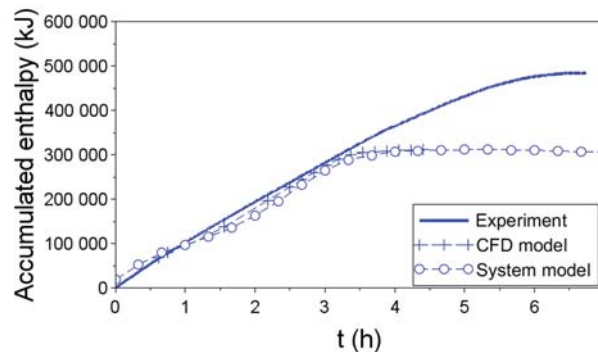


FIGURE 6. Enthalpy accumulated in the PCM, the tube and the fins during the heat charge test led on the experimental module

For  $t < 3.5$ h, both models have a good agreement with the experiment; the discrepancy between the experiment and the system model is between 20 000 and 30 000 kJ, which is 6 to 17% of the experimental result depending on the time instant. After  $t = 3.5$ h, the accumulated energy is stabilized for both models, while it keeps increasing experimentally. This could be due to the layer of PCM that lies between the tube bundle and the external wall of the module, called passive PCM, which is not represented in the models. As it is situated far from the finned tubes, the fusion of passive PCM begins at the moment when the PCM that lies between the fins finishes to melt. The PCM temperature measurements in the prototype module show that this effectively occurs at  $t = 3.5$ h. The thermal energy

that the passive PCM has accumulated at the end of the test can be estimated to be 192 300 kJ, assuming that it has the same final temperature that the rest of the PCM (318°C). The discrepancy between the experiment and the system model on Fig.6 is of 176 400 kJ at the end of the test. The agreement between these two values is quite good, with a relative difference of about 9%; this confirms that the passive PCM is the source of the discrepancy between simulation and experiment after  $t = 3.5$ h. The computational time of the system model for the full charge is about 90 times shorter than the CFD model: this shows once again that the system model is able to reproduce the CFD results with a considerably lower computational effort.

## CONCLUSIONS

The multi-scale approach that is proposed in this work for the numerical modelling of a shell-and-tube LHS system for the storage of steam has been successfully deployed and tested on the case of a prototype scale steam storage module, available at CEA Grenoble. Two main results can be highlighted from the present work.

The first one is that the study of the prototype module with the CFD model showed that it is possible to establish a local 1D correlation for the heat transfer between the liquid water / steam HTF and the PCM during PCM fusion (heat charge). The obtained correlation can therefore be used in a 1D design model that predicts the liquid water length at the bottom of the tubes; this capability is crucial for a design model to correctly estimate the global heat transfer.

The second result is that the generic system model that was built, which integrates the heat transfer correlation extracted from the CFD study, gives satisfying results. The system model correctly reproduces the transient heat transfer rate that the CFD model predicts during the melting of the PCM. Moreover, the modelling approach was validated on experimental results from the prototype module: the system model reproduces the heat transfer rate measured experimentally for a test of steam charge operated in sliding pressure, with a reasonable accuracy ( $\approx 10\%$ ). No tuning of the system model parameters is needed when simulating a new storage charge case, and the computational times are 10 to 90 times shorter than those of the CFD model. This demonstrates the pertinence of the proposed modelling approach for establishing a design model of a storage module.

The work on this multi-scale modelling approach is still ongoing at CEA Grenoble. First, the validation of the system model continues on test charges of the prototype module with non-uniform and non-constant conditions on the HTF side. Second, several improvements could be brought to the methodology. The vertical heat transfer by natural convection in the liquid PCM is currently not taken into account; however this phenomenon may become significant when the tube wall temperature is non-uniform. Also, a simplified system model without radial discretization of the PCM is being investigated, with the goal to gain even more computational time. Finally, the methodology could be extended to steam discharge, which involves liquid water ebullition on the HTF side, and PCM solidification. The methodology will then be able to build a complete design model of a storage module, covering both the charge and discharge processes, and predicting the transient performances accurately and in a reasonable time.

## SYMBOLS

### Latin symbols

$A_{mush}$	mushy zone constant ( $\text{kg}\cdot\text{m}^{-3}\cdot\text{s}^{-1}$ )	$r$	radial position in cylindrical coordinates (m)
$c_p$	heat capacity ( $\text{J}\cdot\text{kg}^{-1}\cdot\text{K}^{-1}$ )	$R$	radius (m)
$D$	thermal diffusivity ( $\text{m}^2\cdot\text{s}^{-1}$ )	$Ra$	Rayleigh number
$g, \vec{g}$	gravity acceleration ( $\text{m}\cdot\text{s}^{-2}$ )	$Re$	Reynolds number
$h$	mass enthalpy ( $\text{J}\cdot\text{kg}^{-1}$ )	$S$	heat exchange surface ( $\text{m}^2$ )
$l_c$	characteristic length (m)	$T$	temperature ( $^{\circ}\text{C}$ )
$L$	latent heat ( $\text{J}\cdot\text{kg}^{-1}$ )	$\vec{v}$	speed ( $\text{m}\cdot\text{s}^{-1}$ )
$\dot{m}$	mass flow ( $\text{kg}\cdot\text{s}^{-1}$ )	$x_m$	PCM mass fraction
$Nu$	Nusselt number	$x_v$	PCM volume fraction
$P$	pressure (pa)	$Y_l$	liquid mass fraction
$q$	heat flux density ( $\text{W}\cdot\text{m}^{-2}$ )	$z$	axial position in cylindrical coordinates (m)

### Greek symbols

$\alpha$	heat-transfer coefficient ( $\text{w.m}^{-2}.\text{k}^{-1}$ )	<i>eq</i>	equivalent
$\beta$	thermal expansion coefficient ( $\text{k}^{-1}$ )	<i>ext</i>	outer boundary of the computational domain
$\phi$	heat flux density ( $\text{w.m}^{-2}$ )	<i>h</i>	homogeneous material
$\Phi$	heat flux ( $\text{w}$ )	<i>i</i>	generic mesh cell (axial direction)
$\lambda$	thermal conductivity ( $\text{w.m}^{-1}.\text{k}^{-1}$ )	<i>in</i>	inner radius of tube
$\mu$	dynamic viscosity( $\text{pa.s}$ )	<i>j</i>	generic mesh cell (radial direction)
$\nu$	kinematic viscosity ( $\text{m}^2.\text{s}^{-1}$ )	<i>l</i>	liquid phase
$\rho$	density ( $\text{kg.m}^{-3}$ )	<i>w</i>	wall
		<i>tube</i>	tube
		<i>ref</i>	reference
		<i>s</i>	solid phase
		<i>sens</i>	sensible
<b>Subscripts</b>			
<i>pc</i>	phase change		
<i>e</i>	outer radius of the tube		

### REFERENCES

1. A. Fernández-García, E. Zarza, L. Valenzuela, and M. Pérez, [Renewable and Sustainable Energy Reviews](#) **14**, 1695-1721 (2010).
2. J. Birnbaum, T. Hirsch, M. Eck, R. Pitz-Paal, M. Fichtner, and G. Zimmermann, "A concept for future parabolic trough based solar thermal power plants," in *15th International Conference on the Properties of Water and Steam* (Berlin, Germany, 2008).
3. P. Garcia, V. Vuillerme, M. Olcese, and N. El Mourchid, [AIP Conference Proceedings](#) **1734**, 050015 (2016).
4. A. Caron-Soupart, J.-F. Fourmigué, P. Marty, and R. Couturier, [Appl. Therm. Eng.](#) **98**, 1286-1296 (2016).
5. M. Martinelli, F. Bentivoglio, A. Caron-Soupart, R. Couturier, J.-F. Fourmigue, and P. Marty, [Appl. Therm. Eng.](#) **101**, 247-261 (2016).
6. R. Bayón, E. Rojas, L. Valenzuela, E. Zarza, and J. León, [Appl. Therm. Eng.](#) **30**, 2643-2651 (2010).
7. D. Laing, C. Bahl, T. Bauer, D. Lehmann, and W.-D. Steinmann, [Solar Energy](#) **85**, 627-633 (2011).
8. P. Garcia, M. Olcese, and S. Rougé, [Energy Procedia](#) **69**, 842-849 (2015).
9. M. Lacroix, [Solar Energy](#) **50**, 357-367 (1993).
10. H.A. Adine and H. El Qarnia, [Applied Mathematical Modelling](#) **33**, 2132-2144 (2009).
11. S.S. Mostafavi Tehrani, Y. Shoraka, G. Diarce, and R.A. Taylor, [Renewable Energy](#) **132**, 694-708 (2019).
12. J.L. Wright, [ASHRAE Transactions](#) **102, Part 1**, 940-946 (1996).
13. S.W. Churchill and H.H.S. Chu, [International Journal of Heat and Mass Transfer](#) **18**, 1323-1329 (1975).
14. W.-W. Wang, L.-B. Wang, and Y.-L. He, [Applied Energy](#) **138**, 169-182 (2015).
15. V.R. Voller, M. Cross, and N.C. Markatos, [Int. J. Numer. Meth. Engng.](#) **24**, 271-284 (1987).
16. V.R. Voller and C. Prakash, [International Journal of Heat and Mass Transfer](#) **30**, 1709-1719 (1987).
17. A. Lomonaco, D. Haillot, E. Pernot, E. Franquet, and J.-P. Bédécarrats, [Solar Energy Materials and Solar Cells](#) **149**, 81-87 (2016).
18. D. Laing, T. Bauer, N. Breidenbach, B. Hachmann, and M. Johnson, [Applied Energy](#) **109**, 497-504 (2013).
19. W.H. Mac Adams, *Transmission de La Chaleur* (Dunod, 1975).
20. V. Gnielinski, [Int. Chem. Eng.](#) **16**, 359-368 (1976).
21. W. Nusselt, *Die Oberflächenkondensation Des Wasserdampfes* (VDI, 1916).
22. S.S. Kutateladze, *Fundamentals of Heat Transfer* (Academic Press, New York, 1963).
23. D.A. Labuntsov, [Teploenergetika](#) **4**, 72-80 (1957).